Journal of Alloys and Compounds 1056 (2026) 186530

Contents lists available at ScienceDirect

Journal of Alloys and Compounds

journal homepage: www.elsevier.com/locate/jalcom

Tunable phase transformation temperature and excellent superelasticity in as-printed NiTiCu shape memory alloys fabricated by the laser powder bed fusion

Bailiang Qin [a], Yongyun Zhang [b], Ze Pu [c], Changyong Chen [a], K.C. Chan [a,*]

[a] Research Institute for Advanced Manufacturing, Department of Industrial and Systems Engineering, The Hong Kong Polytechnic University, Hong Kong, China
[b] Department of Mechanical Engineering, The University of Hong Kong, Pokfulam Road, Hong Kong, China
[c] School of Mechanical Engineering, Shandong University, Jinan 250061, China

ARTICLE INFO

Keywords:
NiTiCu Shape memory alloys
Phase transformation behavior
Additive manufacturing
Superelasticity

ABSTRACT

Shape memory alloys (SMAs) fabricated via additive manufacturing (AM) not only provide a feasible way to build components with complex shapes but also pioneer 4D printing applications due to their unique functional properties. However, the evolution of martensitic transition behavior and superelasticity in NiTiCu SMAs, especially in relation to process parameters and their underlying mechanisms, remains unclear. In this work, a novel $Ni_{46}Ti_{49}Cu_5$ SMA fabricated via laser powder bed fusion (LPBF) exhibit outstanding functionality with a tunable phase transformation temperature without post-heat treatment. By systematically varying laser power (75–250 W), scanning speed (500–1500 mm/s), and hatch spacing (40–110 μm), we identified a distinct input energy density window (62.5–78.13 J/mm^3) that achieves high relative density while eliminating cracks and minimizing porosity. Microstructural analysis reveals columnar grains formed by epitaxial growth along the maximum thermal gradient, resulting in a pronounced < 001 > crystallographic texture on the plane perpendicular to the build direction. The phase transformation temperatures change nearly monotonically with input energy density, primarily due to evaporation of Ni and Cu during processing, which alters the equivalent (Ni+Cu) content of the matrix. The input energy density also strongly influences the superelastic response by controlling porosity. The alloy fabricated with an energy density of 69.44 J/mm^3 yields exceptional superelasticity, with a recovery ratio of 95.33 % and a recoverable strain of 5.72 %. Notably, the phase transformation behavior of the $Ni_{46}Ti_{49}Cu_5$ SMA can be precisely tailored by adjusting processing parameter combinations while maintaining a constant energy density. These findings establish a framework for fabricating NiTi-based SMAs with superior superelasticity and tunable phase transformation temperatures via LPBF, enabling their potential application in advanced smart materials.

1. Introduction

Shape memory alloys (SMAs) represent a remarkable class of functional materials characterized by their ability to recover substantial deformations through reversible phase transformations between austenite and martensite phases [1,2]. Among these, NiTi-based alloys have dominated industrial and biomedical applications due to their exceptional shape memory effect, superelasticity, biocompatibility, and corrosion resistance [3–5]. Recent studies have further highlighted their potential for solid-state refrigeration, owing to a significant elastocaloric effect [6].

Additive manufacturing (AM) has emerged as a new approach for fabricating NiTi SMAs, particularly in the context of 4D printing [7]. By leveraging computer-aided design, AM enables the direct fabrication of intricate geometries without post-processing machining. Nevertheless, the rapid melting and solidification dynamics inherent in AM introduce unique challenges for NiTi alloys, including compositional inhomogeneity due to elemental evaporation (particularly Ni), pore formation, crack initiation, and uncontrolled texture development [8]. With decades of development in the field, significant progress has been made. For example, the ideal input energy density level has been reported frequently for different AM methods, such as laser powder bed fusion (LPBF), directed energy deposition (DED), or electron beam wire-feed additive manufacturing (EBAM) [9–12]. Moreover, the AM

* Corresponding author.
E-mail address: kc.chan@polyu.edu.hk (K.C. Chan).

https://doi.org/10.1016/j.jallcom.2026.186530
Received 18 November 2025; Received in revised form 20 January 2026; Accepted 29 January 2026
Available online 31 January 2026

technology also provides a feasible way to tailor the phase transformation temperature and other functional properties by carefully altering the process parameters to control evaporation of Ni during the process, which is attributed to the unique characteristic of near equiatomic NiTi SMAs, given the extreme sensitivity of near-equiatomic NiTi alloys to compositional shifts (e.g., a 0.1 at% Ni loss can reduce transformation temperatures by ~10 K) [13]. However, a critical unresolved challenge is the poor fatigue life of most AM-fabricated NiTi SMAs, which remains a barrier for applications such as elastocaloric cooling [10,14].

Compared with binary NiTi SMAs, the NiTiCu ternary SMAs exhibit superior fatigue property, functional stability, and narrow thermal hysteresis [15–17]. With similar chemical and physical properties, Cu can substitute up to 30 at% Ni for equiatomic NiTi SMAs while retaining the shape memory effect and superelasticity [18]. Notably, it is reported that when the Cu content exceeds 7.5 %, the B19 martensitic phase occurs, resulting in a shifted phase transformation path from B2 ↔ B19' to B2 ↔ B19 ↔ B19' [19]. The metastable B19 phase with an orthorhombic structure exhibits smaller thermal hysteresis compared with the monoclinic B19' phase. The reduction of thermal hysteresis enhances functional stability by minimizing the accumulation of elastic strain energy and the formation of irreversible defects [20,21]. Even at low Cu concentrations, the incorporation of Cu improves lattice compatibility between austenite and martensite, further stabilizing cyclic performance [22,23].

Recent studies have explored AM-fabricated NiTiCu SMAs. Shiva et al. first reported NiTiCu SMAs fabricated by LPBF with three different Cu contents (5 %, 15 %, and 25 %) using a pre-mixed elemental powder [24–26]. The phase transformation behavior, surface roughness, and mechanical properties of SMAs with different Cu additions fabricated by AM were preliminarily explored. It was found that the as-printed $Ni_{45}Ti_{50}Cu_5$ exhibited an extremely low thermal hysteresis of 1.48 K, compared with the other two high-Cu-content samples. However, due to the rapid solidification process during AM, the addition of a third element Cu, typically leads to elemental segregation, resulting in a heterogeneous structure, especially for pre-mixed elemental powders [27–29]. It was found that even with only 1 at% Cu addition, there was still a Cu segregation at the melt pool boundaries, leading to the coexistence of B19 and R phase [30]. Zheng et al. investigated the thermal stability and shape memory effect in a $Ni_{40}Ti_{50}Cu_{10}$ SMA using L-DED [29] with pre-alloyed powder. Excellent thermal stability was achieved in their work by introducing Ti_2Cu precipitates in the twin ridge to hinder dislocation movements. However, excessive Cu addition leads to a brittle mechanical behaviour [31]. While some studies report superelasticity in AM-fabricated NiTiCu, high recovery ratios typically require pre-training or post-treatment [27,32]. Furthermore, although process parameter optimization has been explored to minimize defects, such as cracks or delamination [27,32], it is essential to further enhance its functional properties and to understand the effects of process parameters on these properties, including phase transformation behavior and superelasticity.

To this end, this study comprehensively investigates the correlations among LPBF processing parameters, microstructural evolution, phase transformation behavior, and superelasticity in a $Ni_{46}Ti_{49}Cu_5$ SMA. The slightly (Ni, Cu)-rich composition is intended to compensate for Ni evaporation during the LPBF process, which is frequently reported in NiTi-based SMAs [33–35]. We elucidate the effects of individual parameters, including laser power, scanning speed, and hatch spacing, on densification, texture development, and superelastic performance. The growth mechanisms of column grain with strong $< 001 >$ crystallographic texture under high thermal gradients during LPBF are revealed. Phase transformation temperatures are demonstrated to be tunable using various combinations of process parameters. Exceptional superelasticity, with a high recovery ratio and recoverable strain, is achieved in the as-printed condition without any post-heat treatment. This work establishes a processing-microstructure-property framework to fabricate high relative density NiTiCu SMA by LPBF with tailored functional properties, paving the way for their deployment in geometrically complex elastocaloric cooling systems and biomedical devices.

2. Experimental procedure

2.1. Powder characterization

The pre-alloy powders $Ni_{46}Ti_{49}Cu_5$ (Liaoning Guanda New Materials Technology Co., LTD, China) for LPBF were fabricated by the plasma rotating electrode process to prevent carbon contamination. The NiTiCu powders exhibit good sphericity, as shown in Fig. 1a. The actual chemical composition of the powder is shown in Table 1. The powder size distribution measured by a particle analyzer (Malvern Mastersizer 3000) ranges from 5 μm to 90 μm, with d_{50} and d_{90} values of 39.6 μm and 66.2 μm, respectively (Fig. 1b). Fig. 1c shows the phase transformation behavior of NiTiCu powders from −150 °C to 150 °C. Two successive phase transformation peaks are observed during both heating and cooling, attributed to inhomogeneities within or among the powders [35]. The main peak temperature of austenite transformation at 22 °C indicates the (Ni, Cu)-rich nature of the powder.

2.2. LPBF process

A commercial LPBF system (SLM 125, Nikon) equipped with a 400 W fiber laser and an 80 μm beam size was used to fabricate the $Ni_{46}Ti_{49}Cu_5$ SMA operating in continuous wave mode. A schematic of the LPBF process parameters is shown in Fig. 1d. The NiTiCu samples were fabricated on an equiatomic NiTi substrate with preheating at 200 °C. To minimize oxygen contamination, the O_2 content in the chamber was reduced to < 10 ppm by continuous purging with high-purity (> 99.999 %) argon gas throughout the printing process. A stripe scanning strategy with an inter-layer rotation angle of 67° was employed (Fig. 1d). Different laser powers (P) from 75 to 250 W, laser scanning speeds (v) from 500 to 1500 mm/s, and hatch spacing (h) from 40 to 110 μm were employed, while the layer thickness ($t = 30$ μm) was kept constant. Samples with different P, v, and h are denoted as batch P, batch v, and batch h. All process-parameter combinations are listed in Table 2. The parameters were selected based on the reported optimal process windows for binary NiTi alloys [35]. The printed samples are shown in Fig. 1e.

2.3. Characterization techniques

In this work, the morphology of defects, melt pools, and grain structure was analyzed using an optical microscope (OM, ZEISS Axiolab 5) with a ZEISS Axiocam 208 color microscopy camera, and a scanning electron microscope (SEM, ThermoFisher Apreo 2S SEM). An energy-dispersive spectrometry (EDS, Oxford Ultim Max) system was used to assess the chemical composition and preliminarily identify second phases. Samples for OM and SEM observation were mechanically polished on a Struers Tegramin-25 auto-polishing machine and chemically etched in a solution of HF (10 vol%), HNO_3 (40 vol%), and H_2O (50 vol %) for 30 s. Electron backscattered diffraction (EBSD, Oxford Symmetry S3) was used to study grain morphology and orientation. EBSD samples were mechanically polished and then electrolytically etched in a solution of CH_3COOH (21 %): $HClO_4$ (79 %). Transmission electron microscope (TEM, FEI-Talos F200 X) coupled with a Super-X™ EDS detector at 200 kV was used to qualitatively examine second phases. TEM samples were ground to ~80 μm, punched into 3 mm disks, and thinned using a Struers TenuPol-3 twin-jet electro-polisher in CH_3OH (90 %): $HClO_4$ (10 %). The relative density of the as-printed samples was measured using Archimedes' method, with a theoretical maximum density of 6.45 g/cm^3. Rectangular samples (3 mm × 3 mm × 6 mm) were measured four times with a Vibra balance equipped with a density

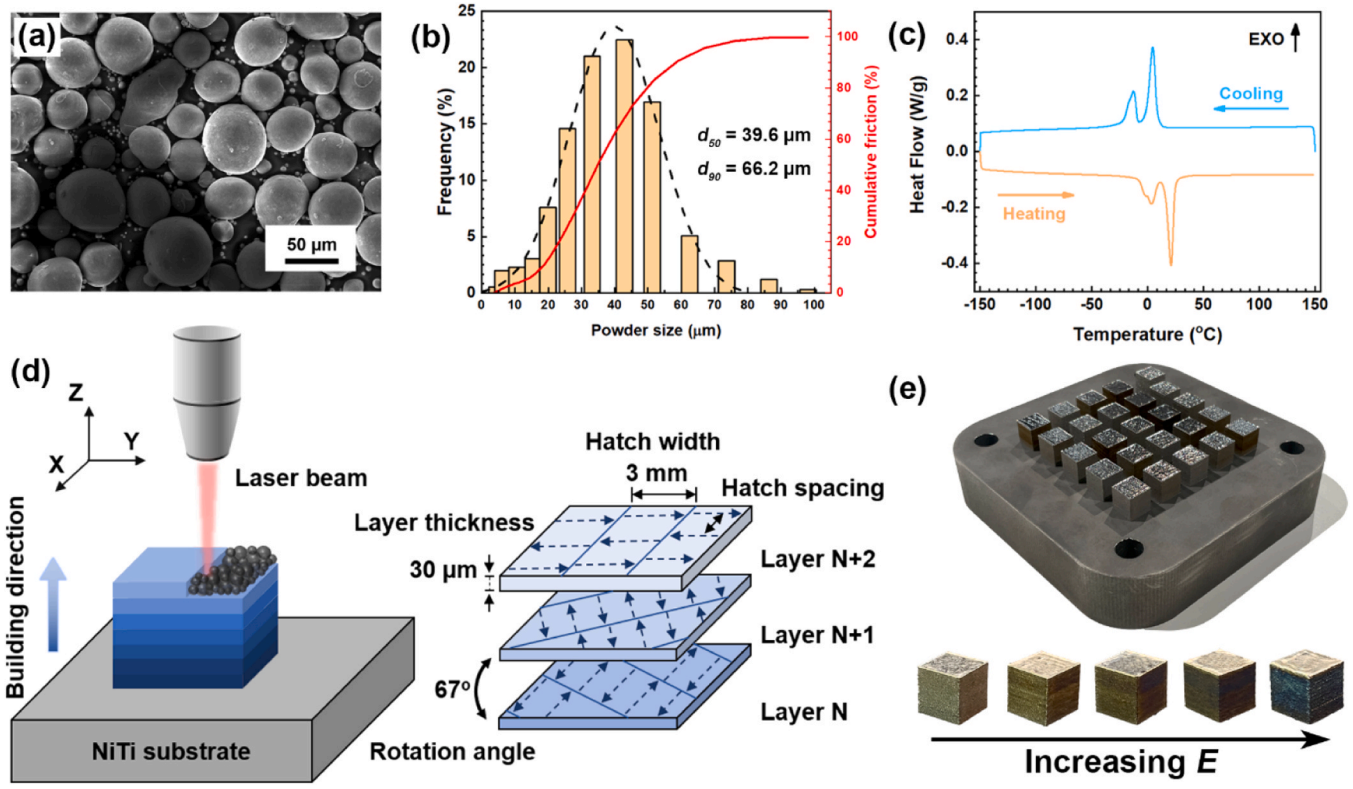

Fig. 1. Powder information and printing method (a) SEM image of NiTiCu pre-alloy powders; (b) the powder size distribution; (c) DSC curves of the NiTiCu pre-alloy powder; (d) the schematic diagram of LPBF additive manufacturing; (e) photos of printed samples.

Table 1
The chemical composition of NiTiCu alloy powder.

Element (at%)	Ni	Ti	Cu	N	C	O
Powder	45.81	49.08	5.08	-	< 0.01	0.03

Table 2
The detailed SLM process parameters for NiTiCu alloy samples.

Number	Laser Power, P (W)	Scanning Speed, v (mm/s)	Hatch Spacing, h (μm)	Layer thickness, t (mm)	Energy input, E (J/mm3)
P1	250	1000	60	0.03	138.89
P2	225	1000	60	0.03	125.00
P3	200	1000	60	0.03	111.11
P4	175	1000	60	0.03	97.22
P5	150	1000	60	0.03	83.33
P6	125	1000	60	0.03	69.44
P7	100	1000	60	0.03	55.56
P8	75	1000	60	0.03	41.67
V1	150	500	80	0.03	125.00
V2	150	666	80	0.03	93.84
V3	150	700	80	0.03	89.29
V4	150	900	80	0.03	69.44
V5	150	1000	80	0.03	62.50
V6	150	1100	80	0.03	56.82
V7	150	1200	80	0.03	52.08
V8	150	1300	80	0.03	48.08
V9	150	1500	80	0.03	41.67
H1	150	800	40	0.03	156.25
H2	150	800	50	0.03	125.00
H3	150	800	60	0.03	104.17
H4	150	800	70	0.03	89.29
H5	150	800	80	0.03	78.13
H6	150	800	90	0.03	69.44
H7	150	800	100	0.03	62.50
H8	150	800	110	0.03	56.82

measurement kit. Unless otherwise noted, all microstructural and phase characterization samples were taken from the mid-height region of the as-printed NiTiCu alloys.

The phase transformation behavior was characterized using differential scanning calorimetry (DSC; TA DSC 250) between −150 °C and 150 °C at a heating/cooling rate of 10 °C/min. Specimens were stabilized at 150 °C for 3 min, cooled to −150 °C and held for 3 min, then reheated to 150 °C and held for 3 min. The superelasticity of the as-printed specimens was evaluated using a universal testing machine (Zwick/Roell Z020) with a temperature-controlled chamber. Cyclic compression to 6 % strain was performed at a low strain rate of 1×10^{-4} s^{-1} at various temperatures using a Zwick video extensometer. The compression direction was along the build direction (Z axis of samples, Fig. 1d). Compression specimens were rectangular columns (3 mm × 3 mm × 6 mm) extracted from the central region of the as-printed samples.

3. Results

3.1. Microstructure

To study the printability of the $Ni_{46}Ti_{49}Cu_5$ SMA, the dependence of relative density (with a theoretical density of 6.46 g/cm^3) on input energy density is shown in Fig. 2. The input volumetric energy density was calculated by the following equation [33]: $E_V = P / (v \times h \times t)$, where P, v, h and t represent the laser power, scanning speed, hatch spacing and layer thickness, respectively. Based on the relative density of the printing samples, three regions with different process parameters were identified. Regions I, II, and III represent the lack-of-fusion region, defect-free region, and keyhole instability region, respectively. In region I, the defects are mainly unmelting powders and lack-of-fusion pores due to the insufficient melt, while the types of defects are micro-cracks and pores in region III as shown in Fig. 2. A distinct process window (Region II) emerged where the relative density exceeded 99.2 %, peaking

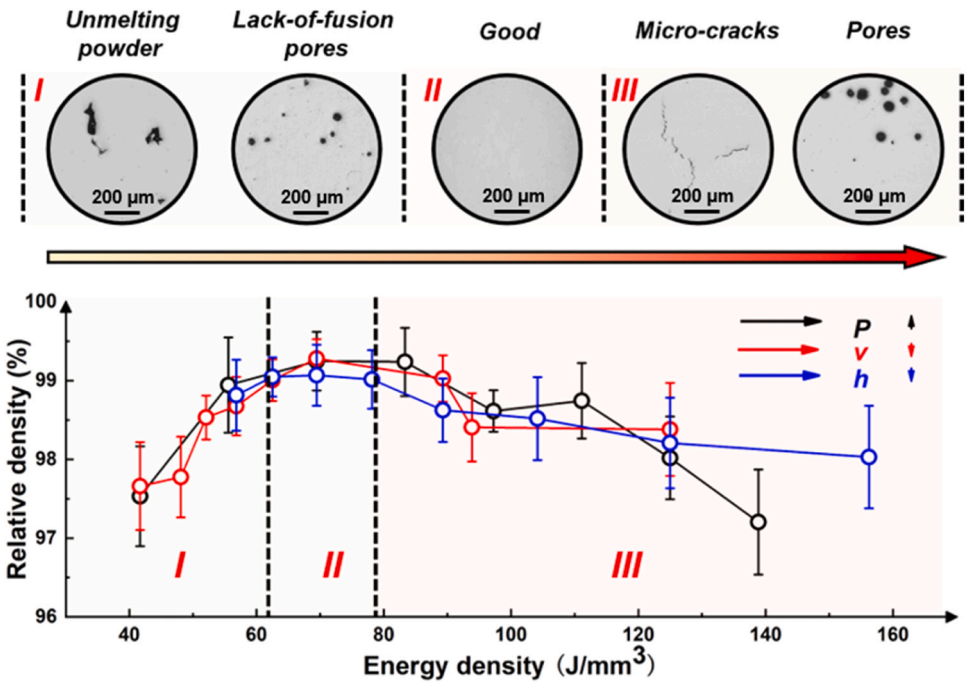

Fig. 2. The process window of the $Ni_{46}Ti_{49}Cu_5$ SMA and different types of defects.

between 62.5 – 78.13 J/mm³ (> 99.0 %) across all parameter sets.

To further reveal the microstructure evolution of as-printed $Ni_{46}Ti_{49}Cu_5$ samples with different process parameters and energy densities, Fig. S1-S3 present unetched microstructures along the build direction (BD). At fixed scanning speed (1000 mm/s) and hatch spacing (60 μm), increasing laser power from 75 to 250 W reveals distinct defect regimes (Fig. S1). Sample P1 (250 W, $E_V = 138.9$ J/mm³) exhibits severe thermal cracking (red cycles in Fig. S1a), resulting in the lowest relative density (97.53 %) due to thermally induced residual stresses [36]. With decreasing laser power, the volume fraction of microcracks and pores decreases gradually, as shown in Fig. S1. Few pores were observed in the samples fabricated with a laser power of 125 W (sample P6, Fig. S1f). With further reduction of laser power, unmelting powders with irregular shapes were observed due to insufficient energy input, as illustrated by

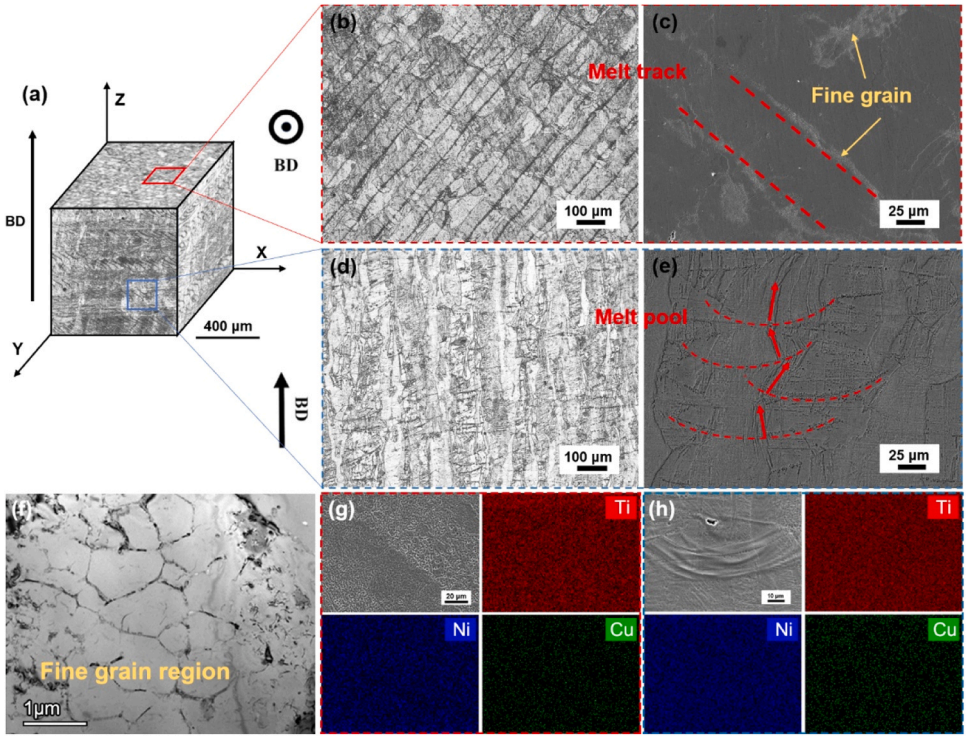

Fig. 3. Microstructure of as-printed V4 sample (a) three-dimensional OM images; (b, c) OM and SEM images of the etched surface perpendicular to the BD and the morphology of melting track; (d, e) OM and SEM images of the etched surface parallel to the BD and the morphology of melt pool; (f) TEM images of regions of fine grain regions; (g, h) EDS mapping of the area around melting tracks and melt pools.

the blue cycles in Fig. S1g and h.

Fig. S2a shows that many pores and microcracks are present in sample V1, fabricated with a low scanning speed v of 500 mm/s ($P = 150$ W and $h = 0.08$ mm). These pores originate from a keyhole structure at high energy density (125 J/mm^3), where vapor recoil forces prevent melt pool collapse, entrapping gases and promoting elemental vaporization [37]. A progressive increase in scanning speed to 700–1000 mm/s substantially reduces defect density (Fig. S2c-f), and the sample with a scanning speed of 900 mm/s shows the highest relative density of 99.28 % among all samples. Conversely, excessive scanning speeds induce lack-of-fusion pores and unmelting powders due to insufficient energy density (Fig. S2h and i).

The microstructure of NiTiCu alloys fabricated with different hatch spacings ($P = 120$ W and $v = 800$ mm/s were fixed) is shown in Fig. S3. Similar to the above P and v groups, small spacings (40 μm, high E_V) generate keyhole porosity, while large spacings (110 μm, low E_V) cause lack-of-fusion voids. The highest densification (99.06 % relative density) occurs at a hatch spacing of 100 μm (H6, Fig. S3f). Interestingly, the number of microcracks of H2 was obviously lower than in samples with the same energy density (P2 and V1), while the number of pores was clearly higher. This phenomenon suggests hatch spacing uniquely modulates thermal stress distribution through altered Marangoni convection patterns [38].

To elucidate orientation-dependent microstructural features, Fig. 3 presents a three-dimensional schematic of the as-printed sample V4 with the building direction (BD) indicated. From the cross-sections perpendicular to the BD (Fig. 3a and c), distinct melt track boundaries are observed, where fine-grained regions are concentrated (<1 μm grain size, Fig. 3f). On the surface along the BD (Fig. 3d and e), epitaxially grown columnar grains aligned with the thermal gradient are evident, as indicated by the red arrows. EDS mapping was performed in the melting track and melt pool regions (Fig. 3g and h), revealing homogeneous element distribution in these regions without obvious elemental segregation.

To investigate the grain size, morphology, and orientation, EBSD characterization was performed on the as-printed NiTiCu samples, as shown in Fig. 4. Inverse pole figure (IPF) maps relative to the building direction (BD) reveal distinct microstructural anisotropy. On the plane perpendicular to BD (Fig. 4a), columnar grains dominate with a pronounced < 001 > texture with a concentration of 8.33, evidenced by the IPF triangle below Fig. 4a. Conversely, the plane parallel to BD (Fig. 4b) exhibits a bimodal < 001 > /< 101 > orientation distribution, indicated by mixed red and green grains. This preferential < 001 > alignment arises from competitive epitaxial growth during layer-by-layer deposition. Partial remelting under large thermal gradients enables newly solidified grains to inherit the crystallographic orientation of previously solidified grains, favoring columnar growth along the < 001 > direction due to its minimized interfacial energy and optimal heat dissipation [39]. The corresponding pole figures in Fig. 4e also exhibit a maximum intensity of 10.36 for the (100) texture from the surface perpendicular to BD.

Grain size distributions differ significantly between orientations: 198.93 μm parallel to BD versus 75.74 μm perpendicular to BD (Fig. S4a and b). Grain boundary analysis indicates 64.5 % low-angle grain boundaries (LAGBs, <15°) perpendicular to BD, compared to 47.6 % parallel to BD (Fig. S4c and d). Kernel Average Misorientation (KAM) maps (Fig. 4d and e) reveal heterogeneous dislocation distributions on both surfaces from the two directions. For the surface perpendicular to BD, a higher volume fraction of dislocations was found in the edge area of the melt track (region A) than in the center area of the melt track (region C), which correlates with the presence of fine cellular substructures at solidification fronts. Interestingly, similar heterogeneity was observed on the surface parallel to BD, where fewer dislocations were found in region C and more were concentrated in region D (Fig. 4d). Fig. 4e exhibits the IPF map of surface perpendicular to the BD of V3. Similarly, V3 shows a strong texture orientation in < 001 > //BD, but with weaker texture intensity of 6.77, which will be discussed later.

To further investigate the precipitation and phase information, TEM

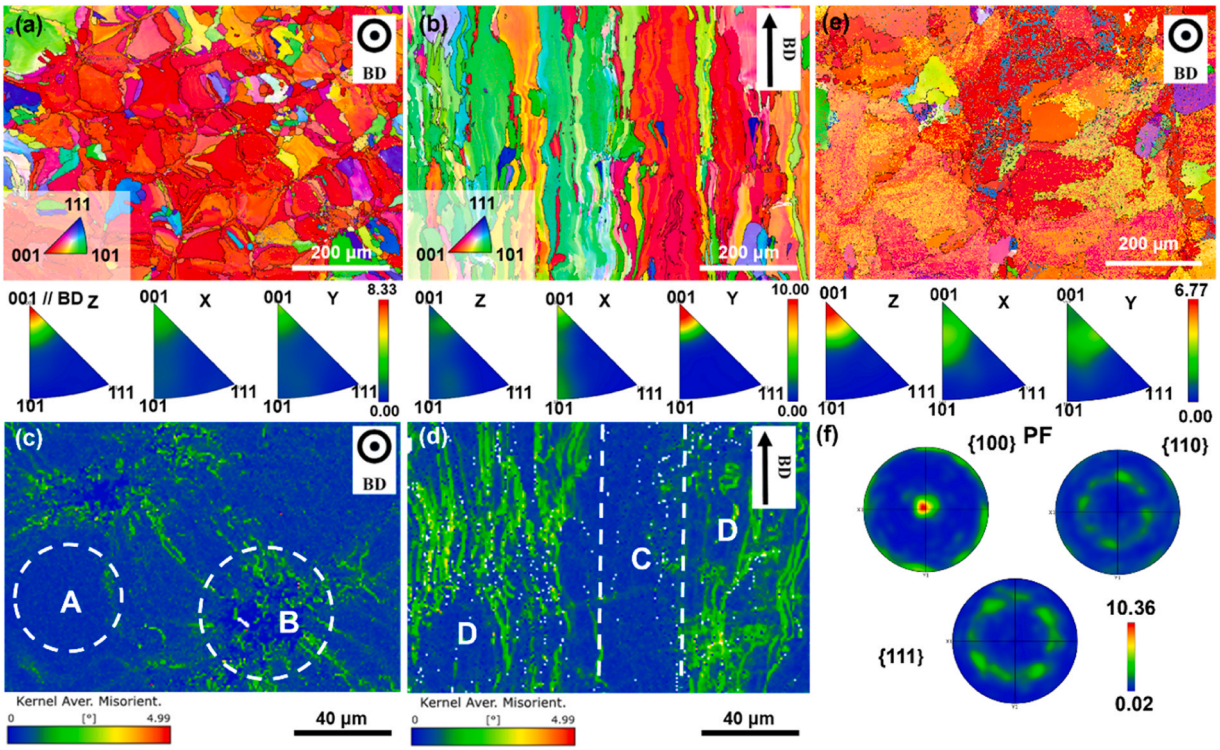

Fig. 4. EBSD analysis of the as-printed NiTiCu samples (a, b) inverse pole-figure map of surface perpendicular and parallel to the BD, respectively of V4; (c, d) KAM images of surface perpendicular and parallel to the BD, respectively. (f) inverse pole-figure map of surface perpendicular to the BD of V3 (e) Pole-figure map of the surface perpendicular to the BD of V4.

analysis was performed in the as-printed NiTiCu sample (V4), as shown in Fig. 5. Striped martensite and round nanoscale precipitates were observed in the as-printed V4 sample and are marked by blue and yellow circles, respectively (Fig. 5a). In addition, massive dislocations (marked by green arrows) are also distributed randomly in the matrix. The corresponding selected area electron diffraction (SAED) patterns of martensite, marked by a red circle in Fig. 5a, confirmed that the martensitic phase is B19 and the matrix is the B2 phase. To further identify the martensitic phase in our SMA, high-resolution TEM images are shown in Fig. 5d. According to their corresponding inverse FFT images (Fig. 5e and f), the lattice fringe spacing for $(110)_{B2}$ and $(011)_{B19}$ are 0.2118 nm and 0.3112 nm, respectively. These values were in agreement with the lattice spacing of 0.3122 nm for the $(011)_{B19}$ rather than 0.3065 nm for the $(011)_{B19'}$ [40]. This indicates the phase transformation path is B2-B19 in our AM-fabricated $Ni_{46}Ti_{49}Cu_5$ SMA.

It was also observed in Fig. 5 that numerous, nearly spherical nanoscale precipitates with diameters smaller than 50 nm (Fig. 5d) are diffusely distributed throughout the matrix. Similar precipitates were identified in other samples, such as V1 (Fig. 6a) and V8 (Fig. 6c). It should be noted that the size of these precipitates in samples with high energy density (V1, 125 J/mm^3) is slightly larger than that in samples fabricated with low energy density (V8, 48.08 J/mm^3) due to the longer exposure time in high temperature [41]. These nanoprecipitates were determined as $Ni_2Ti_4O_x$ phases based on the SAED patterns shown in Fig. 6e. The corresponding EDS mapping results (Fig. 6f) indicate that enrichment of Ti and O in the precipitates, accompanied by depletion of Ni and Cu. $Ni_2Ti_4O_x$ precipitates are commonly observed oxides in AM-fabricated NiTi/NiTiCu SMAs, due to the high affinity of Ti to oxygen. The effects of these precipitates on phase transformation behavior and superelasticity are discussed later in the following section.

Fig. 7 shows the structural evolution during martensitic transformation upon cooling. The diffraction profiles at 343 K and 313 K correspond to the B2 parent phase. At 253 K and below, the reflections confirm the presence of B19 martensite through comparison with standard PDF cards, indicating the occurrence of martensitic transformation. Compared with the B19' phase, the B19 phase exhibits a characteristic peak at 64.3° corresponding to the (200) plane, which is consistent with our TEM results.

3.2. Phase transformation behavior

The phase transformation behavior of as-printed $Ni_{46}Ti_{49}Cu_5$ samples fabricated with different parameters (listed in Table 2) was analysed by DSC and shown in Fig. 8. According to the DSC curves, all samples exhibit a single peak during the heating or cooling process, which is confirmed as B2 ↔ B19 phase transformation behavior based on our microstructure analysis at room temperature. Fig. 8a shows that the transformation peaks of the as-printed samples shift gradually to higher temperatures with increasing beam power (from 75 W to 250 W). A similar trend is also observed in batches of *v* and *h*; the transformation peaks shift toward high temperatures with increasing input energy density either by increasing *v* or decreasing *h* (Fig. 8b and c). Notably,

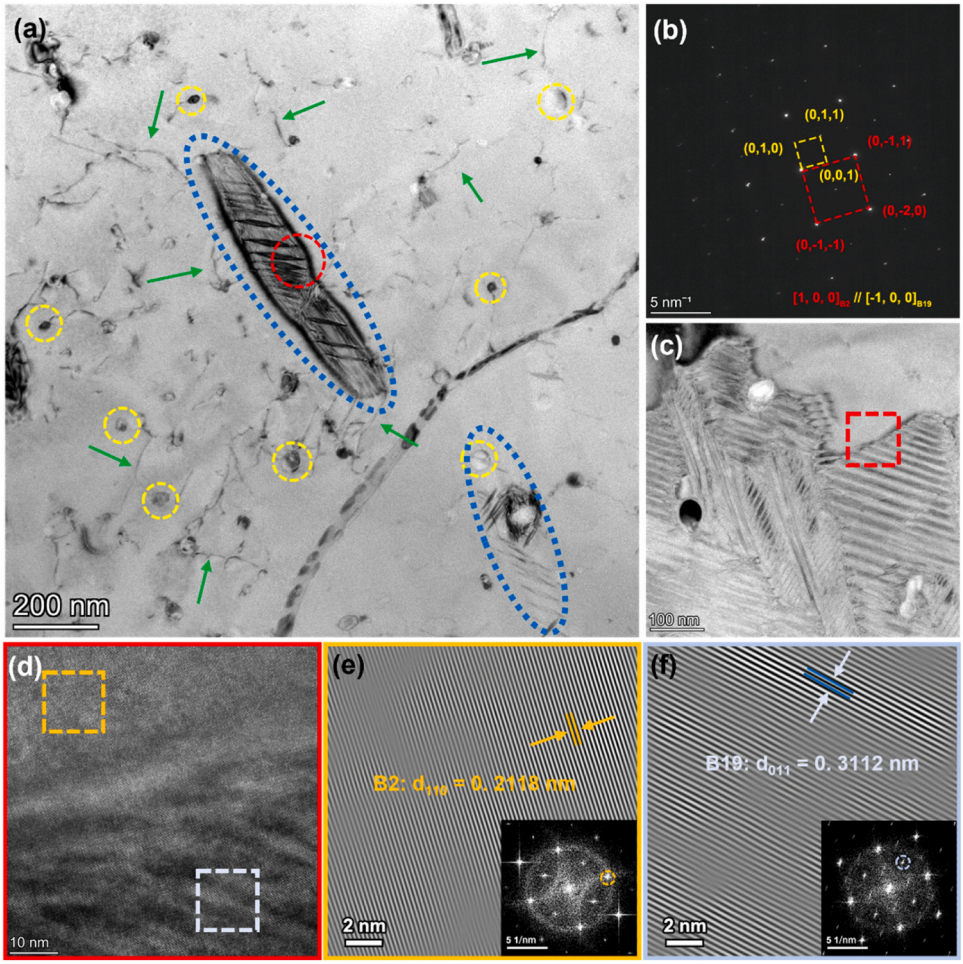

Fig. 5. TEM images of as-printed V4 NiTiCu sample (a) bright field of martensite, dislocation and nanoprecipitations; (b) SAED pattern of selected area marked by the red circle in (a); (c) bright field of martensite; (d) high-resolution TEM of the selected region marked by the red rectangle in (c); (e) IFFT images in the selected region marked by the yellow rectangle in (d); (f) IFFT images in the selected region marked by the blue rectangle in (d).

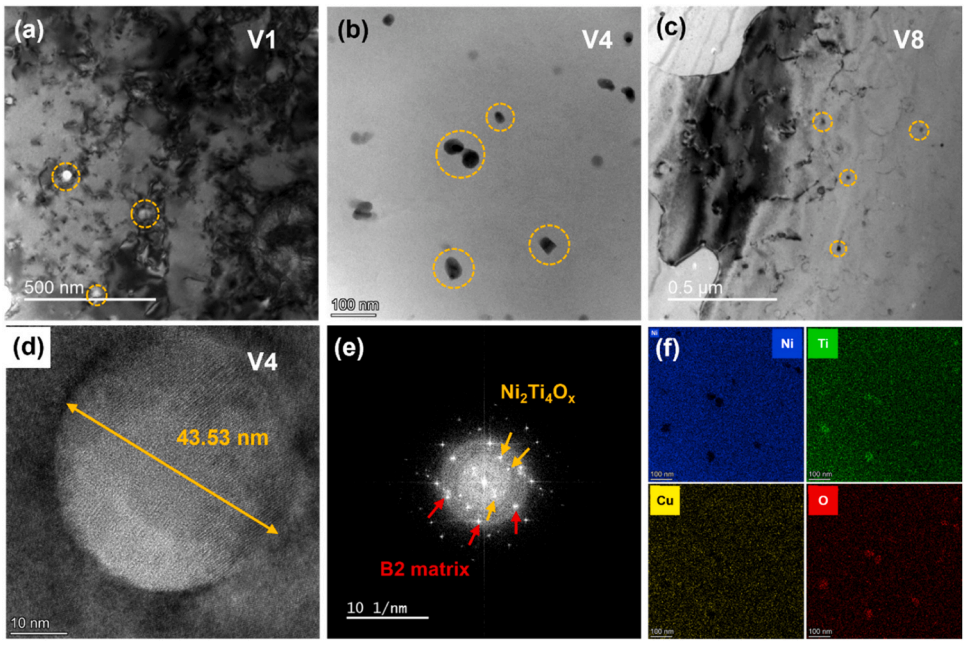

Fig. 6. TEM images of nanoprecipitates in the as-printed NiTiCu samples (a) V1; (b) V4; (c) V9; (d, e) HRTEM image and corresponding FFT images of nanoprecipitates in V4; (d) EDS mapping of (b).

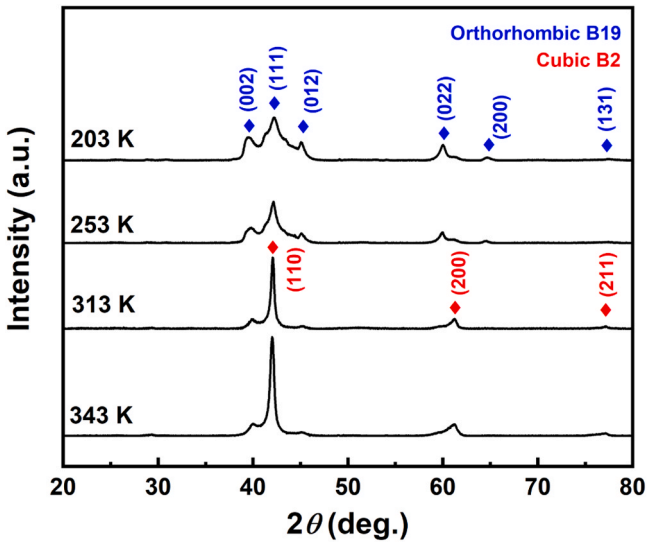

Fig. 7. XRD patterns of as-printed V4 sample at different temperatures.

specimens fabricated at or below 60 μm hatch spacing display broadened, flattened transformation peaks indicative of microstructural heterogeneity [42]. Additionally, it is observed that the transformation interval is reduced and the peak becomes sharper as the energy density increases.

Fig. 8 also summarizes the dependence of phase transformation characteristics on the input energy density across three parameter batches. The starting, peak, and ending temperatures of the martensitic transformation and its reverse transition, denoted by M_s, M_p, M_f, and A_s, A_p, A_f, are determined using the tangent method on DSC curves. According to Fig. 8d-f, transformation temperatures of as-printed samples during forward and reverse martensitic transformation increase nearly monotonically with energy density for all parameter groups. However, the dependency of phase transformation temperature on different process parameters varies. For example, the M_p temperature increases 46.06 K (Figs. 8d) and 16.99 K (Fig. 8e) with the same increase in input energy density of 83.33 J/mm^3 (from 41.67 J/mm^3 to 125.00 J/mm^3) by controlling power and scanning speed, respectively. When controlling the energy density by hatch spacing, A_f and M_s are observed to increase with increasing the energy density, while M_s, M_p, M_f, and A_p first increase and then decrease when the energy density exceeds 89.29 J/mm^3 due to the inhomogeneous microstructure (Fig. 8f), thereby broadening the transformation peaks [7].

Since the transformation enthalpy and thermal hysteresis are also useful for analysing phase transformation behavior and specific applications, their evolution with input energy density is shown in Fig. S5. The transformation enthalpies of the martensitic transformation (ΔH_M) and austenite transformation (ΔH_A), determined by integrating the peak area, exhibit a near-linear relationship with energy density, as shown in Fig. S5a. The transformation enthalpy is in the range of 18–26 J/g, which is comparable to that of NiTiCu fabricated by conventional methods, indicating a complete martensitic or austenitic transformation of our as-printed $Ni_{46}Ti_{49}Cu_5$ SMA [43]. The thermal hysteresis, originating from the energy barriers at the austenite-martensite interface, is a critical parameter for SMAs due to its direct correlation with functional fatigue [20]. In addition, the thermal hysteresis (determined by A_p - M_p) ranges from 16 K to 20 K, with a slight increasing trend as the energy density increases, as shown by the fitting lines in Fig. S5b.

3.3. Superelasticity

The superelastic response of as-printed $Ni_{46}Ti_{49}Cu_5$ SMA was systematically evaluated through 10 compressive loading-unloading cycles at $A_f + 10$ K, as shown in Fig. 9 and Fig. S6-S8. It can be found that all samples exhibit superelasticity with different levels of residual strain (ε_{ir}) and recoverable strain (ε_r). The residual and recoverable strains are indicated by the red lines shown in Fig. 9a. The recovery ratio (η_r) is defined as $\frac{\varepsilon_r}{\varepsilon_t} \times 100\%$, where ε_t represents the applied strain (near 6 % for all samples). According to Fig. S6, NiTiCu samples fabricated with high laser power (250 – 150 W) exhibited moderate superelasticity with a similar residual strain and strain recovery rate in the first cycle. P5 (P = 150 W) exhibits the best superelasticity in the batch *P* with a residual strain of 0.52 % and a recovery rate of 91.19 % in the first cycle (Fig. 9b) and a total recovery ratio of 73.45 % after 10 cycles. When power is decreased to 75 W, the superelasticity deteriorates severely

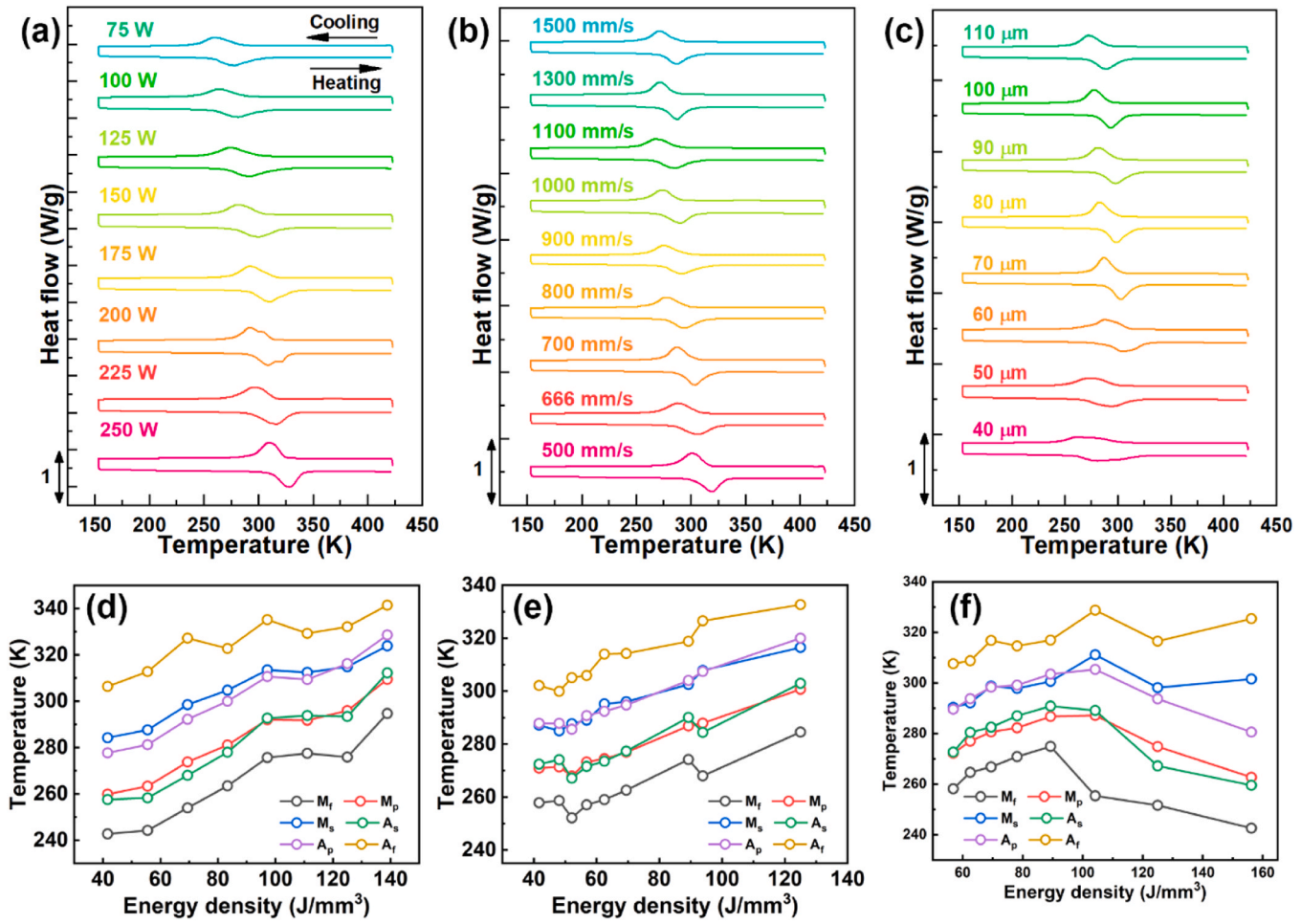

Fig. 8. Phase transformation behavior of NiTiCu alloys fabricated by LPBF with different process parameters: DSC curves of (a) batch *P*; (b) batch *v*; (c) batch *h*, and the dependence of phase transformation temperature on input energy density: (d) batch *P*; (e) batch *v*; (f) batch *h*.

with only a 64.09 % recovery ratio in first cycle and a total recovery ratio of 44.12 % after 10 cycles as shown in Fig. 9c. For samples in the batch *v*, the V1 exhibited a normal superelasticity with a recovery ratio of 84.71 % and 62.81 % at first cycle and 10th cycle respectively (Fig. 9d). With increasing *v*, the recovery ratio keeps increasing until reaching to 95.33 % (1st cycle) and 84.43 % (10th cycle) of the V4 sample, which is the best superelasticity among all samples as shown in Fig. 9e. The V9 sample with an energy density of 41.67 J/mm^3 shows the worst superelasticity with only 33.32 % recovery ratio after ten cycles. In the H group, when $h = 100$ μm (H6, Fig. 9h), the largest recovery ratio of 93.99 % with excellent stability was achieved.

The dependency of recovery ratio and critical stress (σ_c) of as-printed NiTiCu samples on energy density is shown in Fig. 10. It is shown that even though the residual strain gradually accumulates with cycling, almost all samples are able to fully recover after 10 cycles, as indicated by blue lines in Fig. 9. So, the total recovery ratio was recorded to reflect the different functional stability of as-printed samples in Fig. 10. The recovery ratio first increases and then decreases with increasing input energy density for all three batches. The high superelastic performance occurs in an energy density range similar to that of its counterpart, corresponding to a high relative density. For batch *P*, the total recovery ratio remains stable at approximately 70 % within a wide energy density range of 65–130 J/mm^3. In batch *v*, three samples (from 56.82 J/mm^3 to 69.44 J/mm^3) exhibit a recovery ratio of over 90 % in the first cycle and 80 % after 10 cycles, indicating good superelasticity and stability. The great superelastic responses are observed in an energy density range of 62.5–89.29 J/ mm^3 for batch *h*. Notably, extreme energy density values yield severely compromised superelasticity, as exemplified by the V9 (41.67 J/mm^3) and H1 (156.25 J/mm^3) samples, which exhibit a total recovery ratio of less than 40 % after 10 cycles.

Notably, samples with identical energy density but different parameter combinations exhibit significant variations in performance. For example, the smaller recovery ratio of the P6 compared to the V4 and the H6, all fabricated with the same energy density of 69.44 J/mm^3, is attributed to a relatively lower density (due to more defects) and other microstructural features. This suggests that different parameter combinations may further improve superelasticity.

4. Discussion

4.1. The effect of process parameters on the melt pool

The melt pool morphology plays an important role in determining microstructure formation during the solidification process, including defect generation and texture orientation. Previous work reported that the melt pool shape is primarily governed by the linear energy density (E_L, calculated as P/v) based on single-track experiments. The hatch spacing (h) is typically considered more influential for thermal history than melt pool shape [44,45]. However, the h can also influence the shape of the melt pool for printing bulk samples, as shown in Fig. 11a. The reduced h values (increasing E_V) lead to simultaneous increases in both melt pool width and depth. The half-width and depth of the melt pool were increased from 83.96 μm and 47.39 μm of H8 sample (E_V = 83.96 J/mm^3) to 93.09 μm and 116.87 μm of H3 sample (E_V =

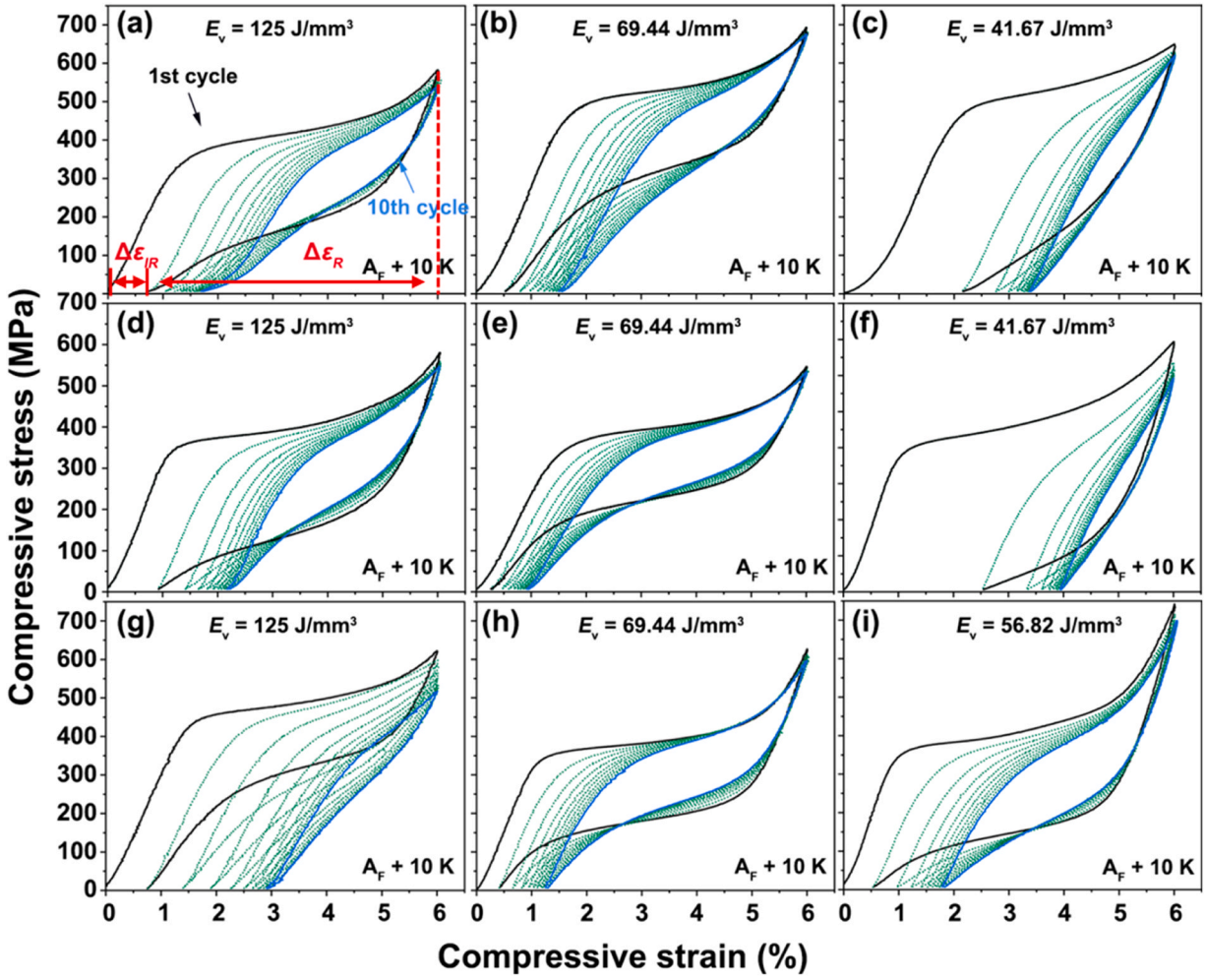

Fig. 9. Superelasticity of as-printed samples tested at A_f + 10 K: (a) P2;(b) P6; (c) P7; (d) V1;(e) V4;(f) V9; (g) H2; (h) H6; (i) H8.

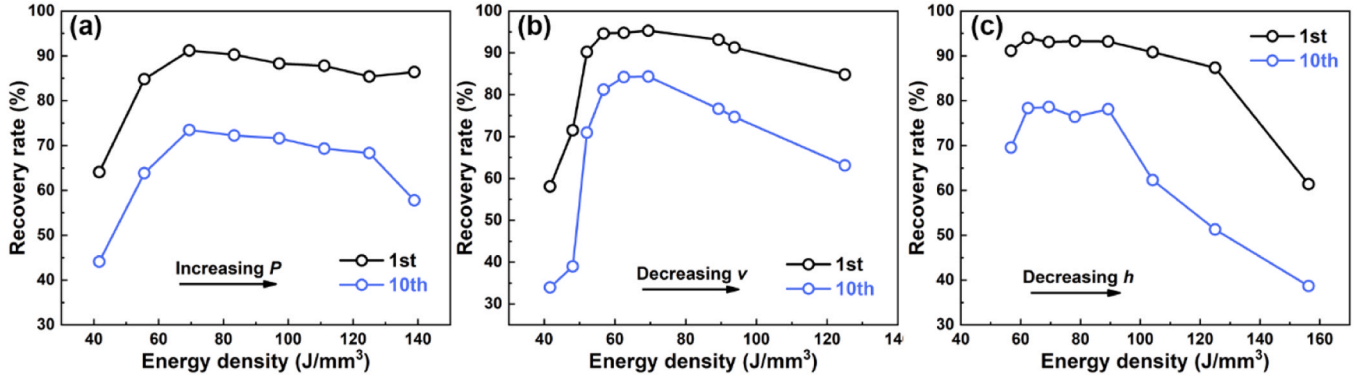

Fig. 10. The dependence of recovery rate on E_V (a) batch *P*; (b) batch *v*; and (c) batch *h*.

104.17 J/mm^3). Besides, the melt pool morphology shifts from the bowl shape toward keyhole structures due to increased overlap regions and residual heat accumulation. Thus, the E_V, which incorporates the effect of hatch spacing, provides a more comprehensive metric for melt pool design. A schematic evolution of melt pool morphology with increasing E_V is shown in Fig. 11b. At low E_V values, melt pools exhibit a shallow morphology with flat bottoms, which is generally favorable for minimizing defect formation. However, excessively low E_V reduces pool width, leading to insufficient overlap between adjacent tracks and resulting in lack-of-fusion pores or unmelted powder [41,46]. Moreover, balling may occur due to inadequate liquid formation and high surface tension. With increasing E_V, the depth and width of the melt pool gradually increase, and defects, such as lack-of-fusion pores or unmelted powder, also disappear gradually (Fig. 11a$_2$). In high E_V mode, the melt pool geometry transitions to a keyhole structure (Fig. 11a$_3$), resulting in increased porosity due to gas bubble entrapment within the vapor depression zone [10,47]. Additionally, the steep thermal gradients in high EV mode further promote the accumulation of residual stress, which can lead to thermal cracking or delamination. Based on our experimental results, the input energy density for fabricating a high

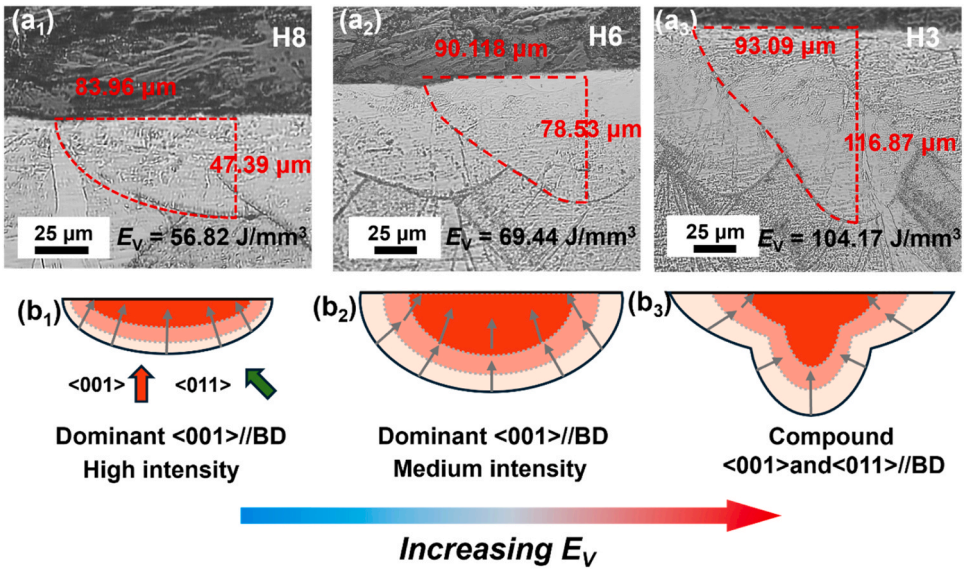

Fig. 11. Schematic of melt pool morphology and the mechanism of grain growth direction under different printing parameters: (a) OM images of melt pool morphology; (b) schematic of melt pool evolution with E_V.

relative density component was determined to be 69.44 J/mm^3 among three groups with a flat bottom melt pool (Fig. 11a).

The morphology not only influences the formation of printing defects, but also the texture orientation of printed samples. While the $< 001 >$ direction typically dominates under maximal thermal gradients in cubic crystals [10], the orientation of the largest thermal gradient is tunable by varying the process parameters. The evolution of texture orientation with E_V is shown in Fig. 11b. In low E_V mode, due to the shallow depth of the melt pool, the highest thermal gradient is largely toward the printing surface, leading to a high concentration of $< 001 >$ orientation texture. With increasing E_V, the depth and width of the melt pool gradually increase, leading to a shift in the growth direction from $< 001 >$ to $< 011 >$, especially on both sides of the melt pool (Fig. 11b$_2$). Further increasing E_V, the keyhole structure occurs and gradually shifts to the largest thermal gradient from the printing surface to the melt pool core, resulting in a higher fraction of $< 011 >$ texture (Fig. 11b$_3$). This explains that the stronger $< 001 >$ texture intensity in samples fabricated with higher energy density in Fig. 4. For example, the $< 011 >$ direction of a near-single-crystal aligned with the build direction in AM 316 L steel was achieved in a high-energy-density keyhole structure [47]. Building on this, Xue et al. investigated the influence of the adjacent melt pool on crystal orientation evolution and fabricated a pseudo-single-crystal $< 001 > /< 011 >$ texture in NiTi SMAs [10] under low E_L regimes.

In fact, texture orientation is influenced not only by adjacent tracks but also by the previously printed layers. During processing, epitaxial growth at the overlap between the molten region and the earlier printed track or layer inherits the existing crystal orientation, leading to a slight difference in growth orientation between the current melt pool and the prior one [10]. This multiscale inheritance mechanism explains why the printing strategy has a significant impact on texture development. For example, the 'X-scan pattern' with 0° inter-layer rotation maintains perfect orientation inheritance, enabling near-single-crystal $< 001 >$ growth [47]. In contrast, our process strategy with 67° inter-layer rotation (Fig. 1d) was designed to mitigate thermal accumulation and minimize defects, but it necessarily introduces crystallographic misalignment between successive layers. This controlled misorientation produces the observed $< 001 >$ or $< 011 >$ texture in the plane parallel to BD (Fig. 4b), where competing growth directions emerge according to local thermal gradient orientations during solidification.

4.2. Tunable phase transformation temperature

The phase transformation behavior of as-printed $Ni_{46}Ti_{49}Cu_5$ samples is shown to be highly influenced by process parameters. While all sample exhibits a single stage B2 ↔ B19 martensitic transition during the heating and cooling process, the phase transformation characteristics, such as transformation temperature, enthalpy change and thermal hysteresis, vary with energy density (Fig. 8). For most samples, the phase transformation temperature increases with rising energy density (increasing P or decreasing v or h), which is attributed to the extreme sensitivity to Ni content in Ni-rich NiTi-based SMAs [33]. According to Frenzel et al., in near-equiatomic NiTiCu SMAs, the M_s temperature remains strongly dependent on the equivalent (Ni + Cu) content when x_{Ni+Cu} exceeds 50 at% [43]. The chemical composition of the printed samples is mainly determined by two factors. First, the evaporation of Cu and Ni elements during printing, especially at high E_V levels, alters the matrix composition. Second, oxide formation during LPBF affects the composition of the matrix and thereby the transformation behaviour. Unlike conventional manufacturing, the layer-by-layer nature of LPBF makes the process particularly sensitive to chamber oxygen levels due to the longer exposure time of the melt pool [8]. Our TEM analysis identifies Ti-rich $Ni_2Ti_4O_x$ as the predominant oxide phase (Fig. 6), due to the higher affinity of Ti to O [35]. These precipitates deplete Ti from the matrix, which would normally decrease transformation temperatures. However, the strict argon atmosphere maintained during the printing process limits oxide volume fraction and particle sizes to below 50 nm (Fig. 6), making their impact secondary to Ni/Cu evaporation.

Fig. 12a exhibits the relation between the transformation temperature A_F and the equivalent (Ni + Cu) content. The A_F decreases as the (Ni + Cu) content increases from 50.0 at% and 51.0 at%, consistent with previous work [43]. Fig. 12b-d illustrates the dependence of Ni, Cu, and the equivalent (Ni + Cu) content on energy density, with the dashed lines representing the fitted results. It is shown that they all decrease linearly with increasing energy density, directly correlating with the observed shifts in transformation temperature. This compositional evolution explains the consistent elevation of phase transformation temperatures across all parameter sets, as reduced (Ni + Cu) content drives the alloy toward Ti-richer compositions with higher transformation temperatures. It has been reported that Ni is more prone to evaporation than Ti in binary NiTi SMAs due to its lower boiling point and higher equilibrium vapor pressure [33]. Similarly, compared with

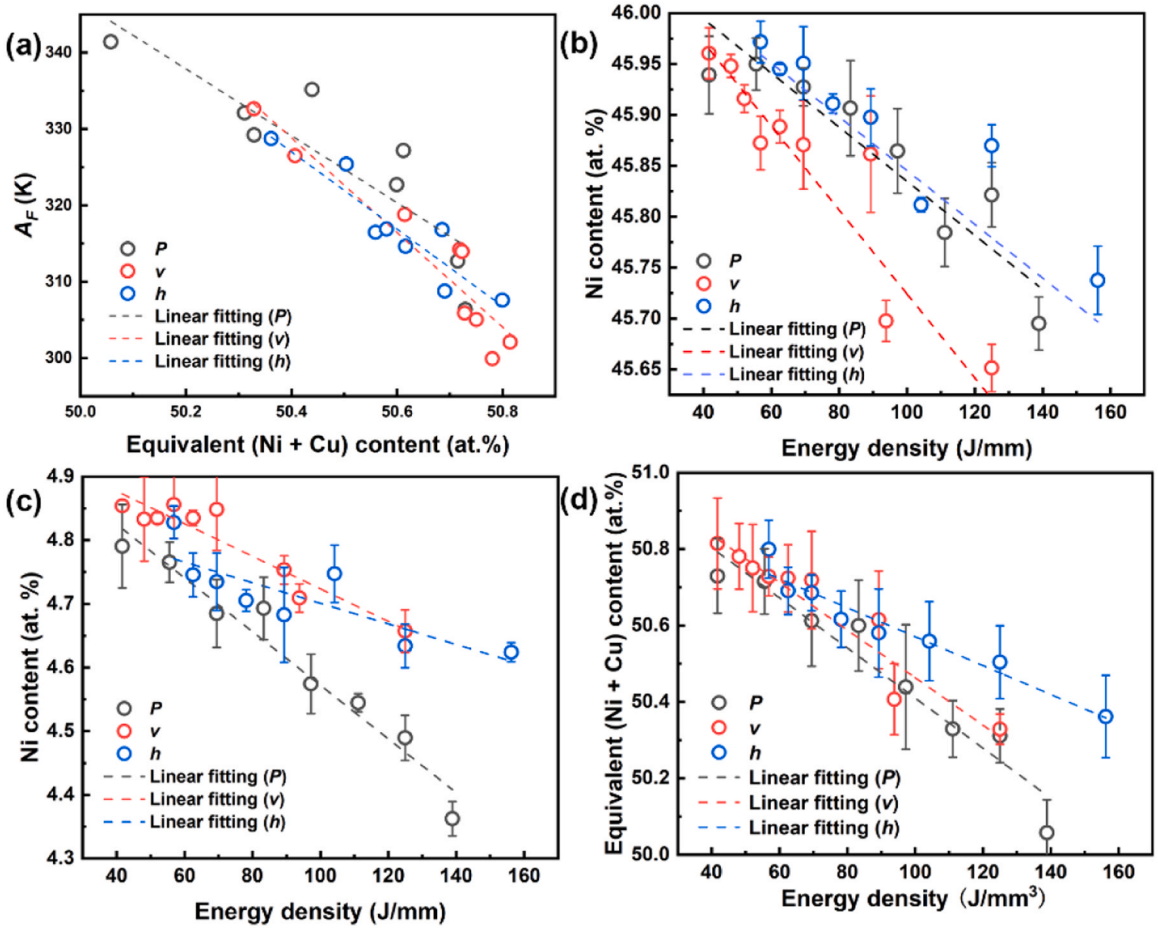

Fig. 12. (a) The dependence of A_F temperature on equivalent (Ni + Cu) content; The dependence of (b) Ni content, (c) Cu content, and (d) equivalent (Ni + Cu) content in the matrix on energy density (dashed lines are the fitted results).

Ti, both Ni and Cu have lower boiling points (at 3003 K and 2835 K, respectively), leading to enhanced evaporation during the LPBF process. In particular, the lower boiling point of Cu leads to slightly higher evaporation than Ni, despite its relatively low addition of 5 at%.

While energy density (E_V) serves as a primary control parameter, individual process variables (laser power (P), scanning speed (v), and hatch spacing (h)) affect the phase transformation temperature differently. For example, for the same increase in energy density ($\Delta E_V \approx 85$ J/mm^3), variations in laser power and scanning speed produce temperature shifts of ~30 K, larger than the ~20 K shifts from hatch spacing adjustments. This differential sensitivity is consistent with prior reports emphasizing the dominant influence of scanning speed on thermal history [33]. Notably, specimens fabricated with identical E_V but different parameter combinations exhibit transformation temperature variations of up to 15 K, indicating that the temperature depends not simply on E_V, but on the joint effect of P, v, and h. These findings enable precise tuning of the transformation temperature through strategic parameter selection for different applications.

The thermal hysteresis, originating from the energy barriers at the austenite-martensite interface, is a critical parameter for SMAs due to its direct correlation with functional fatigue [20]. It reflects energy dissipation during phase transformation, where minimizing the elastic interfacial layer reduces the formation of irreversible defects. The magnitude of thermal hysteresis is fundamentally linked to the middle eigenvalue (λ_2) of the martensitic transformation matrix U, which serves as a quantitative indicator for designing fatigue-resistant SMAs. In the present $Ni_{46}Ti_{49}Cu_5$ SMA, the incorporation of 5 at% Cu reduces thermal hysteresis to below 20 K, a significant improvement over the > 30 K typical of binary NiTi. This reduction indicates enhanced lattice compatibility between phases, attributed to the Cu-induced modification of the transformation strain tensor [17,48]. The lowered thermal hysteresis suggests improved functional stability under cyclic loading compared with binary NiTi SMAs.

4.3. The effect of process parameters on superelasticity

The superelastic performance of as-printed $Ni_{46}Ti_{49}Cu_5$ SMA is fundamentally governed by the microstructure formed during LPBF, including defects, precipitations, and crystallographic texture [49]. Printing defects, such as cracks and pores, are the primary factors affecting the superelastic response, as evidenced by the parallel trends between recovery rate and relative density with increasing energy density, as shown in Figs. 2 and 9. The irrecoverable strain during loading-unloading cycles is mainly attributed to two reasons: plastic deformation via dislocation slip and stabilization of residual martensite through dislocation pinning. The rapid solidification during LPBF generates high intrinsic dislocation densities and heterogeneous residual stress distributions (Fig. 4), which promote the formation of defects. During loading-unloading cycling, elevated local stress near defects further promotes dislocation accumulation, leading to a severe stress concentration [9]. Once the stress exceeds the critical level for dislocation slips, irreversible plastic deformation occurs, producing permanent strain. Concurrently, dislocation networks interact with martensite variants, impeding their reverse transformation and contributing to irrecoverable strain. This explains why superelastic recovery is relatively low in both the low E_V and high E_V modes in our as-printed NiTiCu

samples. However, an appropriate dislocation density is beneficial for achieving optimal superelastic recovery in the alloys. Conventionally processed NiTiCu alloys typically require mechanical training or cold working to stabilize their superelastic response [50,51]. During pre-training or cold deformation, a large volume fraction of dislocations or remnant martensite is introduced, creating a favorable internal stress for subsequent transformation. As a result, dislocations tend to saturate, and fewer dislocations form, leading to a stable recovery ratio in further cycling.

Interestingly, while large-sized $Ni_2Ti_4O_x$ precipitates are detrimental to ductility, nanosized precipitates (20 −50 nm, Fig. 6) are considered beneficial to superelasticity [10,52]. On the one hand, the elastic strain fields around the nanoprecipitates provide nucleation sites for martensite at the interfaces between the matrix and the precipitates, leading to the lower critical stress for martensite transformation. On the other hand, nanoprecipitates act as barriers to dislocation slips and can suppress irrecoverable strain during cycling, resulting in larger irrecoverable strain. Thus, the combination of high dislocation density and nanoprecipitates contributes to the exceptional superelasticity in our as-printed $Ni_{46}Ti_{49}Cu_5$ SMA. It should be noted that the precipitates contribute mainly to cyclic stability rather than the magnitude of recoverable strain.

The relation between the grain structure, crystal texture, and loading direction is also essential for superelasticity and mechanical properties. According to Sehitoglu et al. [53], a higher recoverable transition strain and lower Schmid factors for austenite slip are found in the [001] and [148] orientations compared with other directions for the compressive test of NiTi single crystal SMAs. As shown in Fig. 4, the as-printed $Ni_{46}Ti_{49}Cu_5$ SMA exhibit a pronounced columnar grain structure with a strong $< 001 >$ texture (Fig. 4), which supports their excellent superelasticity. The unique texture, combined with high relative density and nanoprecipitation, synergistically produces remarkable superelasticity performance, with a 95.33 % recovery ratio, and a 5.72 % recoverable strain in sample V4 without any post-processing. Fig. 13 exhibits the superelastic response of some ternary NiTi-based SMAs fabricated by AM [27,32,54–56]. As compressive results of most reported works are recorded by the stroke of the fixture instead of the extensometer, we also add a data point recorded from the fixture movement, and the stress-strain curve is shown in Fig. S9. It should be noted that the strain derived from fixture movement is larger than that measured by an extensometer, because it includes the displacement of both the sample and the fixture. In Fig. 13, all data obtained using an extensometer are plotted as hollow symbols, while the other data obtained from the fixture movement are plotted as solid symbols. It can be seen that our as-printed NiTiCu SMAs exhibit superior superelastic response among ternary NiTi-based SMAs.

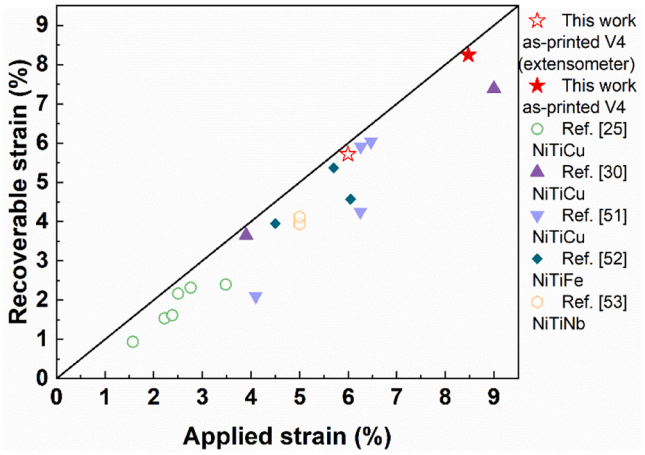

Fig. 13. Comparison of recoverable strain of AM-ed ternary NiTi-based SMAs [27,32,54–56].

5. Conclusion

In the present study, the microstructure evolution, phase transformation behavior, and superelasticity of NiTiCu SMAs fabricated by LPBF were systematically investigated. The main conclusions could be summarized as follows:

(1) The input energy density (E_V) plays an important role in the relative density of the NiTiCu SMAs fabricated by LPBF. An optimized E_V window of 62.5–78.13 J/mm^3 was established to fabricate defect-free NiTiCu SMAs.
(2) Epitaxial growth along maximal thermal gradients produces columnar grains with distinct texture anisotropy. A strong $< 001 >$ crystallographic texture was observed on the surface perpendicular to BD, while a mixed $< 001 >$ and $< 011 >$ texture was found on the surface parallel to BD.
(3) All specimens undergo a single-stage B2↔B19 transformation during DSC. The phase transformation temperature and transformation enthalpy increase monotonically with increasing input energy density, primarily due to the evaporation of Ni and Cu during LPBF.
(4) Superelastic performance exhibits a strong correlation with relative density and energy density. A high recovery ratio of 95.33 % and a recoverable strain of 5.72 % are achieved in the V4 without any post-treatment.
(5) NiTiCu samples fabricated with the same energy density using different combinations of parameters exhibit different relative densities and functional performance. Therefore, all process parameters (P, v, h, and rotation angle) should be carefully designed to achieve the desirable phase transformation temperature and optimal superelasticity.

These results establish a framework for fabricating high-performance NiTiCu SMAs with tailored phase transformation temperature and superelasticity, unlocking their potential for biomedical and elastocaloric applications requiring complex geometries.

CRediT authorship contribution statement

Chan K. C.: Writing – review & editing, Validation, Supervision, Resources, Project administration, Methodology, Funding acquisition, Conceptualization. **Changyong Chen:** Writing – review & editing. **Ze Pu:** Writing – review & editing. **Yongyun Zhang:** Writing – review & editing. **Bailiang Qin:** Writing – original draft, Visualization, Validation, Investigation.

Declaration of Competing Interest

The authors declare that they have no known competing financial interests or personal relationships that could have appeared to influence the work reported in this paper.

Acknowledgements

This work was supported by a grant from the Department of Industrial and Systems Engineering, The Hong Kong Polytechnic University (project code: 4-ZZXF).

Appendix A. Supporting information

Supplementary data associated with this article can be found in the online version at doi:10.1016/j.jallcom.2026.186530.

Data availability

The raw/processed data required to reproduce these findings cannot be shared at this time, as they also form part of an ongoing study.

References

[1] Shape memory and pseudoelastic behavior of 51.5%Ni–Ti single crystals in solutionized and overaged state, Acta Mater. 49 (2001).
[2] B. Kockar, I. Karaman, J.I. Kim, Y.I. Chumlyakov, J. Sharp, C.J. Yu, Thermomechanical cyclic response of an ultrafine-grained NiTi shape memory alloy, Acta Mater. 56 (14) (2008) 3630–3646.
[3] Z. Li, J. Cai, Z. Zhao, Y. Yang, Y. Ren, G. Sha, L. Cui, K. Yu, D. Jiang, Y. Xiao, S. Mao, S. Hao, Local chemical inhomogeneity enables superior strength-ductility-superelasticity synergy in additively manufactured NiTi shape memory alloys, Nat. Commun. 16 (1) (2025) 1941.
[4] P. Hua, M. Xia, Y. Onuki, Q. Sun, Nanocomposite NiTi shape memory alloy with high strength and fatigue resistance, Nat. Nanotechnol. 16 (4) (2021) 409–413.
[5] E. Farber, J.-N. Zhu, A. Popovich, V. Popovich, A review of NiTi shape memory alloy as a smart material produced by additive manufacturing, Mater. Today. Proc. 30 (2020) 761–767.
[6] J. Chen, L. Lei, G. Fang, Elastocaloric cooling of shape memory alloys: a review, Mater. Today Commun. 28 (2021).
[7] J. Ma, B. Franco, G. Tapia, K. Karayagiz, L. Johnson, J. Liu, R. Arroyave, I. Karaman, A. Elwany, Spatial control of functional response in 4D-printed active metallic structures, Sci. Rep. 7 (2017) 46707.
[8] M. Elahinia, N. Shayesteh Moghaddam, M. Taheri Andani, A. Amerinatanzi, B. A. Bimber, R.F. Hamilton, Fabrication of NiTi through additive manufacturing: a review, Prog. Mater. Sci. 83 (2016) 630–663.
[9] Y. Cao, X. Zhou, D. Cong, H. Zheng, Y. Cao, Z. Nie, Z. Chen, S. Li, N. Xu, Z. Gao, W. Cai, Y. Wang, Large tunable elastocaloric effect in additively manufactured Ni–Ti shape memory alloys, Acta Mater. 194 (2020) 178–189.
[10] L. Xue, K.C. Atli, C. Zhang, N. Hite, A. Srivastava, A.C. Leff, A.A. Wilson, D. J. Sharar, A. Elwany, R. Arroyave, I. Karaman, Laser powder bed fusion of defect-free NiTi shape memory alloy parts with superior tensile superelasticity, Acta Mater. 229 (2022).
[11] H. Hou, E. Simsek, T. Ma, N.S. Johnson, S. Qian, C. Cisse, D. Stasak, N. Al Hasan, L. Zhou, Y. Hwang, R. Radermacher, V.I. Levitas, M.J. Kramer, M.A. Zaeem, A. P. Stebner, R.T. Ott, J. Cui, I. Takeuchi, Fatigue-resistant high-performance elastocaloric materials made by additive manufacturing, Science 366 (6469) (2019) 1116–1121.
[12] Z. Pu, D. Du, K. Wang, G. Liu, D. Zhang, X. Wang, B. Chang, Microstructure, phase transformation behavior and tensile superelasticity of NiTi shape memory alloys fabricated by the wire-based vacuum additive manufacturing, Mater. Sci. Eng. A 812 (2021).
[13] J. Frenzel, E.P. George, A. Dlouhy, C. Somsen, M.F.X. Wagner, G. Eggeler, Influence of Ni on martensitic phase transformations in NiTi shape memory alloys, Acta Mater. 58 (9) (2010) 3444–3458.
[14] Y. Wu, E. Ertekin, H. Sehitoglu, Elastocaloric cooling capacity of shape memory alloys – Role of deformation temperatures, mechanical cycling, stress hysteresis and inhomogeneity of transformation, Acta Mater. 135 (2017) 158–176.
[15] E.M. Feygin, C.A. Schuh, Interface compatibility and hysteresis in shape memory materials are affected by lattice distortions from applied stresses, Acta Mater. 283 (2025).
[16] C. Bechtold, C. Chluba, R. Lima de Miranda, E. Quandt, High cyclic stability of the elastocaloric effect in sputtered TiNiCu shape memory films, Appl. Phys. Lett. 101 (9) (2012).
[17] R. Zarnetta, R. Takahashi, M.L. Young, A. Savan, Y. Furuya, S. Thienhaus, B. Maaß, M. Rahim, J. Frenzel, H. Brunken, Y.S. Chu, V. Srivastava, R.D. James, I. Takeuchi, G. Eggeler, A. Ludwig, Identification of quaternary shape memory alloys with near-zero thermal hysteresis and unprecedented functional stability, Adv. Funct. Mater. 20 (12) (2010) 1917–1923.
[18] R. Radhamani, M. Balakrishnan, Predictive modeling of phase transformation temperatures in NiTiCu shape memory alloys: Integrating electronic factors through artificial neural network, Mater. Today Commun. 38 (2024).
[19] S. Cai, J.E. Schaffer, T. Shi, J. Gao, L. Kadeřávek, Effect of Cu alloying and heat treatment parameters on NiTi alloy phase stability and constitutive behavior, Shape Mem. Superelasticity 10 (4) (2024) 460–472.
[20] Y. Song, X. Chen, V. Dabade, T.W. Shield, R.D. James, Enhanced reversibility and unusual microstructure of a phase-transforming material, Nature 502 (7469) (2013) 85–88.
[21] R. Delville, S. Kasinathan, Z. Zhang, J.V. Humbeeck, R.D. James, D. Schryvers, Transmission electron microscopy study of phase compatibility in low hysteresis shape memory alloys, Philos. Mag. 90 (1-4) (2010) 177–195.
[22] J. Cui, Y.S. Chu, O.O. Famodu, Y. Furuya, J. Hattrick-Simpers, R.D. James, A. Ludwig, S. Thienhaus, M. Wuttig, Z. Zhang, I. Takeuchi, Combinatorial search of thermoelastic shape-memory alloys with extremely small hysteresis width, Nat. Mater. 5 (4) (2006) 286–290.
[23] P. Dang, Y. Zhou, J. Pang, X. Ding, J. Sun, T. Lookman, D. Xue, Achieving stable actuation response and elastocaloric effect in a nanocrystalline Ti50Ni40Cu10 alloy, Scr. Mater. 226 (2023).
[24] S. Shiva, nfluence of Cu addition to improve shape memory properties in NiTi alloys developed by laser rapid manufacturing, J. Laser Micro/Nanoeng. 11 (2) (2016) 153–157.
[25] S. Shiva, I.A. Palani, C.P. Paul, S.K. Mishra, B. Singh, Investigations on phase transformation and mechanical characteristics of laser additive manufactured TiNiCu shape memory alloy structures, J. Mater. Process. Technol. 238 (2016) 142–151.
[26] S. Shiva, N. Yadaiah, I.A. Palani, C.P. Paul, K.S. Bindra, Thermo mechanical analyses and characterizations of TiNiCu shape memory alloy structures developed by laser additive manufacturing, J. Manuf. Process. 48 (2019) 98–109.
[27] H. Lu, Z. Zhou, Y. Yang, C. Deng, H. Ma, W. Cai, S. Yin, C. Yang, Superelasticity over a wide temperature range in a NiTiCu shape memory alloy via laser powder bed fusion, Mater. Des. 257 (2025).
[28] F.L. Shen, L.T. Pan, C.C. Li, W.H. Xin, Z. Lyu, X.Y. Fang, L.J. Li, The microstructure and anisotropy of compressive behavior in NiTiCu alloy fabricated by laser powder bed fusion processing, J. Alloy. Compd. 1032 (2025).
[29] Y. Ba, Y. Lv, M. Yan, H. Jin, L. Guo, Q. Zhang, Effect of energy density on mechanical properties of NiTiCu shape memory alloys prepared by SLM, Materials 17 (23) (2024).
[30] F.L. Shen, C.C. Li, T.J. Ma, L.T. Pan, W.H. Xin, S.Z. Niu, X.Y. Fang, Effects of Cu distribution on the transformation temperatures and mechanical behavior of NiTi-based alloys fabricated by laser powder bed fusion and heat treatment, Mater. Sci. Eng. A 933 (2025).
[31] R. Rajeshkannan, B. Muralidharan, S. Pandi Rajasabai, R. Naveenkumar, Mechanical and thermomechanical characterization of Ni50-x Ti50Cux(x = 2, 5, 10at%) with morphological studies, Mater. Today. Proc. 65 (2022) 258–264.
[32] Z. Li, J. Zhong, J. Zhang, B. Song, B. Liu, Y. Shi, L. Zhang, Toward additive manufactured crack-free NiTiCu shape memory alloys with low-hysteresis and tailorable phase transition behavior supported by theoretical design, Addit. Manuf. 92 (2024).
[33] X. Wang, J. Yu, J. Liu, L. Chen, Q. Yang, H. Wei, J. Sun, Z. Wang, Z. Zhang, G. Zhao, J. Van Humbeeck, Effect of process parameters on the phase transformation behavior and tensile properties of NiTi shape memory alloys fabricated by selective laser melting, Addit. Manuf. 36 (2020).
[34] C. Zhao, H. Liang, S. Luo, J. Yang, Z. Wang, The effect of energy input on reaction, phase transition and shape memory effect of NiTi alloy by selective laser melting, J. Alloy. Compd. 817 (2020).
[35] L. Xue, K.C. Atli, S. Picak, C. Zhang, B. Zhang, A. Elwany, R. Arroyave, I. Karaman, Controlling martensitic transformation characteristics in defect-free NiTi shape memory alloys fabricated using laser powder bed fusion and a process optimization framework, Acta Mater. 215 (2021).
[36] S. Parvizi, S.M. Hashemi, F. Asgarinia, M. Nematollahi, M. Elahinia, Effective parameters on the final properties of NiTi-based alloys manufactured by powder metallurgy methods: a review, Prog. Mater. Sci. 117 (2021).
[37] A.N. Alagha, S. Hussain, W. Zaki, Additive manufacturing of shape memory alloys: a review with emphasis on powder bed systems, Mater. Des. (2021) 204.
[38] L. Johnson, M. Mahmoudi, B. Zhang, R. Seede, X. Huang, J.T. Maier, H.J. Maier, I. Karaman, A. Elwany, R. Arróyave, Assessing printability maps in additive manufacturing of metal alloys, Acta Mater. 176 (2019) 199–210.
[39] R. Xi, H. Jiang, G. Li, S. Kustov, Z. Zhang, H. Wei, Z. Liu, G. Zhao, J. Van Humbeeck, X. Wang, In-situ alloying of NiTiNb ternary shape memory alloys via laser powder bed fusion using pre-alloyed NiTi and elemental Nb powders: microstructure, phase transformation behavior and functional properties, Addit. Manuf. 79 (2024).
[40] K. Otsuka, X. Ren, Physical metallurgy of Ti–Ni-based shape memory alloys, Prog. Mater. Sci. 50 (5) (2005) 511–678.
[41] S. Saedi, N. Shayesteh Moghaddam, A. Amerinatanzi, M. Elahinia, H.E. Karaca, On the effects of selective laser melting process parameters on microstructure and thermomechanical response of Ni-rich NiTi, Acta Mater. 144 (2018) 552–560.
[42] Z. Pu, D. Du, D. Zhang, Z. Li, S. Xue, R. Xi, X. Wang, B. Chang, Improvement of tensile superelasticity by aging treatment of NiTi shape memory alloys fabricated by electron beam wire-feed additive manufacturing, J. Mater. Sci. Technol. 145 (2023) 185–196.
[43] J. Frenzel, A. Wieczorek, I. Opahle, B. Maaß, R. Drautz, G. Eggeler, On the effect of alloy composition on martensite start temperatures and latent heats in Ni–Ti-based shape memory alloys, Acta Mater. 90 (2015) 213–231.
[44] J.P. Oliveira, A.D. LaLonde, J. Ma, Processing parameters in laser powder bed fusion metal additive manufacturing, Mater. Des. 193 (2020).
[45] M. Tang, P.C. Pistorius, J.L. Beuth, Prediction of lack-of-fusion porosity for powder bed fusion, Addit. Manuf. 14 (2017) 39–48.
[46] M.H. Nasab, D. Gastaldi, N.F. Lecis, M. Vedani, On morphological surface features of the parts printed by selective laser melting (SLM), Addit. Manuf. 24 (2018) 373–377.
[47] S.-H. Sun, T. Ishimoto, K. Hagihara, Y. Tsutsumi, T. Hanawa, T. Nakano, Excellent mechanical and corrosion properties of austenitic stainless steel with a unique crystallographic lamellar microstructure via selective laser melting, Scr. Mater. 159 (2019) 89–93.
[48] D. Zheng, R. Li, J. Kang, C. Han, T. Yuan, Unveiling ultra-stable cyclic martensitic transformation behavior of an additively manufactured NiTiCu shape memory alloy, Addit. Manuf. 102 (2025).
[49] S. Wei, J. Zhang, L. Zhang, Y. Zhang, B. Song, X. Wang, J. Fan, Q. Liu, Y. Shi, Laser powder bed fusion additive manufacturing of NiTi shape memory alloys: a review, Int. J. Extrem. Manuf. 5 (3) (2023).
[50] Z. Zhao, J. Lin, Y. Xiao, J. Min, Improved superelastic stability by nanosegregation via low-temperature aging in Ti-50.9 at% Ni shape memory alloy, Scr. Mater. 245 (2024).
[51] H. Lin, P. Hua, K. Huang, Q. Li, Q. Sun, Grain boundary and dislocation strengthening of nanocrystalline NiTi for stable elastocaloric cooling, Scr. Mater. 226 (2023).

[52] H.Z. Lu, H.W. Ma, W.S. Cai, X. Luo, Z. Wang, C.H. Song, S. Yin, C. Yang, Stable tensile recovery strain induced by a Ni4Ti3 nanoprecipitate in a Ni50.4Ti49.6 shape memory alloy fabricated via selective laser melting, Acta Mater. 219 (2021).
[53] H. Sehitoglu, I. Karaman, R. Anderson, X. Zhang, K. Gall, H.J. Maier, Y. Chumlyakov, Compressive response of NiTi single crystals, Acta Mater. 48 (13) (2000) 3311–3326.
[54] H. Wang, W. Mann, L. Lan, L. Jiang, Q. Zhang, X. Yan, B. He, Effect of pre-mixed powders on the microstructure and superelasticity of laser directed energy deposited NiTiCu shape memory alloy, J. Mater. Sci. 60 (13) (2025) 5996–6007.
[55] B. Yuan, J.-G. Ge, L. Zhang, H.-J. Chen, L.-S. Wei, Y.-D. Zhou, R.-H. Song, Laser powder bed fusion of NiTiFe shape memory alloy via pre-mixed powder: microstructural evolution, mechanical and functional properties, Rare Met. 43 (5) (2024) 2300–2316.
[56] H. Shen, Q. Zhang, G. Kang, M. Zhou, X. Li, Y. Yang, Z. Zhang, L. Cui, S. Hao, Enhancing thermal stability of laser powder bed fusion fabricated 60NiTi alloy via Nb alloying, Mater. Sci. Eng. A 922 (2025).